Iso-orientation bias of layer 2/3 connections: the unifying mechanism of spontaneous, visually and optogenetically driven V1 dynamics

Tibor Rózsa[1†], *Remy Cagnol*[1†], *Ján Antolík*[1]
[1]*Faculty of Mathematics and Physics, Charles University, Czech Republic*
† These authors contributed equally to this work.

Abstract

Functionally specific long-range lateral connectivity in layer 2/3 of the primary visual cortex (V1) supports the integration of visual information across visual space and shapes spontaneous, visual and optogenetically driven V1 activity. However, a comprehensive understanding of how these diverse cortical regimes emerge from this underlying cortical circuitry remains elusive. Here we address this gap by showing how the same model assuming moderately iso-orientation biassed long-range cortical connectivity architecture explains diverse phenomena, including (i) range of visually driven phenomena, (ii) modular spontaneous activity, (iii) the propagation of spontaneous cortical waves, and (iv) neural responses to patterned optogenetic stimulation. The model offers testable predictions, including presence of slower and iso-tropic spontaneous wave propagation in layer 4 and non-monotonicity of optogenetically driven cortical response to increasingly larger disk of illumination. We thus offer a holistic framework for studying how cortical circuitry governs information integration across multiple operating regimes.

Introduction

A fundamental function of sensory systems is integrating information across sensory space. In vision, this is often studied by sensory stimulation and analysis of lateral interactions between spatially offset cortical sites (*1–3*). However, such sensory-driven approaches often conflate the complexities of feed-forward processing with recurrent lateral interactions. The primary visual cortex (V1) exhibits complex dynamics even without visual input, either during spontaneous activity, or in response to artificial external stimulation, offering an alternative means to study cortical integration without feed-forward confounds. Several phenomena highlight the interconnectedness of visually and non-visually driven dynamics:

Spontaneous travelling waves (STW): Waves of activity propagating across V1 (*4–6*) at speeds consistent with unmyelinated lateral axons (*7*), with propagation biases aligned with cortical functional organisation (*8*), and influencing behaviour (*7*, *9*).
Modular spontaneous activity: Spontaneously emerging activity patterns in V1 are correlated with functional maps (*10*), linking resting-state dynamics with visual coding.

Optogenetically evoked patterns of activity: Optogenetic perturbations of ongoing V1 activity bridge the resting and visually evoked dynamics (*11–14*), offering a way to study cortical interactions without engaging retino-cortical pathways.

Ultimately, visual spatial integration across these cortical regimes (spontaneous, visually driven, and optogenetically driven) relies on a shared neural substrate, especially the functionally specific long-range lateral connectivity in layer 2/3 (*15–17*). Yet, a systematic understanding of how this common substrate supports the diverse computations involved in visual integration, and under different cortical regimes, remains elusive.

Bridging this gap requires a comprehensive approach capable of simultaneously addressing anatomy, network dynamics, and function, which computational models are uniquely suited for. While offering valuable insights, previous computational studies fall short of unifying the full range of dynamical regimes and levels of integration. Recent phenomenological models have shown how modular activity arises spontaneously or through optogenetic stimulation (*10*, *14*), while others investigated travelling waves (*18*), optogenetic stimulation (*19*) or statistics of spontaneous activity (*20*). But all these models did not consider visually specific processing or anatomy. The model of Davis et al. (*9*) included structured connectivity and demonstrated functionally biassed spontaneous activity, but did not link to visually or optogenetically driven processing. Finally, Cai et al. (*21*) demonstrated modular spontaneous activity in a single-layer V1 model, but did not address spontaneous wave propagation or external stimulation.

To explain how V1's shared neural substrate supports spatial visual integration across diverse dynamical regimes, we developed a unified model of columnar V1 (Figure 1B) that accurately simulates visual processing, spontaneous travelling waves, modular spontaneous activity, and functionally specific optogenetic modulation (Figure 1C). Our model replicates (i) distributions of wavelength and propagation speed in spontaneous waves observed in marmoset, along with biases toward iso-oriented propagation seen in macaque and cat V1, (ii) modular spontaneous activity correlated with orientation maps in both excitatory and inhibitory neurons in ferret V1, (iii) impulse-response properties to both full-field homogeneous and patterned optogenetic stimulation in ferret V1, and (iv) range of visually driven phenomena. The model yields testable predictions including slower, functionally independent spontaneous wave propagation in layer 4 and non-monotonic response of neurons in the surround of a disk of optogenetic stimulation that is increasing in diameter. Parametric analysis of the model reveals that functional specific lateral interactions in layer 2/3 are critical for emergence of these spontaneous, visually driven and optogenetically driven phenomena (Figure 1C), unifying an unprecedented range of previously fragmented experimental findings (*4*, *8*, *10*, *12–14*, *18*, *22*). This study advances understanding of how these diverse processes are interlinked, moving towards a holistic understanding of sensory processing in the brain.

Results

Here we present a generic model of columnar V1 derived from our previous work (*23*) (see Methods for full list of changes). It considers the first two stages of V1 processing - the cortical layers 4 and 2/3, each populated by excitatory and inhibitory cells modelled as adaptive exponential integrate-and-fire neurons (Figure 1B). Layer 4 receives input from a phenomenological model of the retino-thalamic pathway, with feed-forward receptive field templates globally organised according to pre-computed retinotopic and orientation preference maps (see Methods). The cortical model circuit follows multiple connectivity rules: the probability of connectivity falls off with distance, intra-layer 4 connectivity follows push-pull organisation, and the long-range layer 2/3 connections exhibit a moderate iso-orientation bias (Figure 1A). The model was calibrated using anatomical and physiological data from cat and macaque, but we demonstrate here that it also explains activity dynamics in marmoset and ferret V1. As its predecessor (*23*, *24*), the new model offers quantitatively accurate account of a broad range of visually evoked phenomena, including orientation tuning of spikes, membrane potential and conductances, distribution of modulation ratios, differences between flashed vs. continuous stimulation, and cross-trial spiking precision modulation by stimulus (see Supplementary figures S1-5).

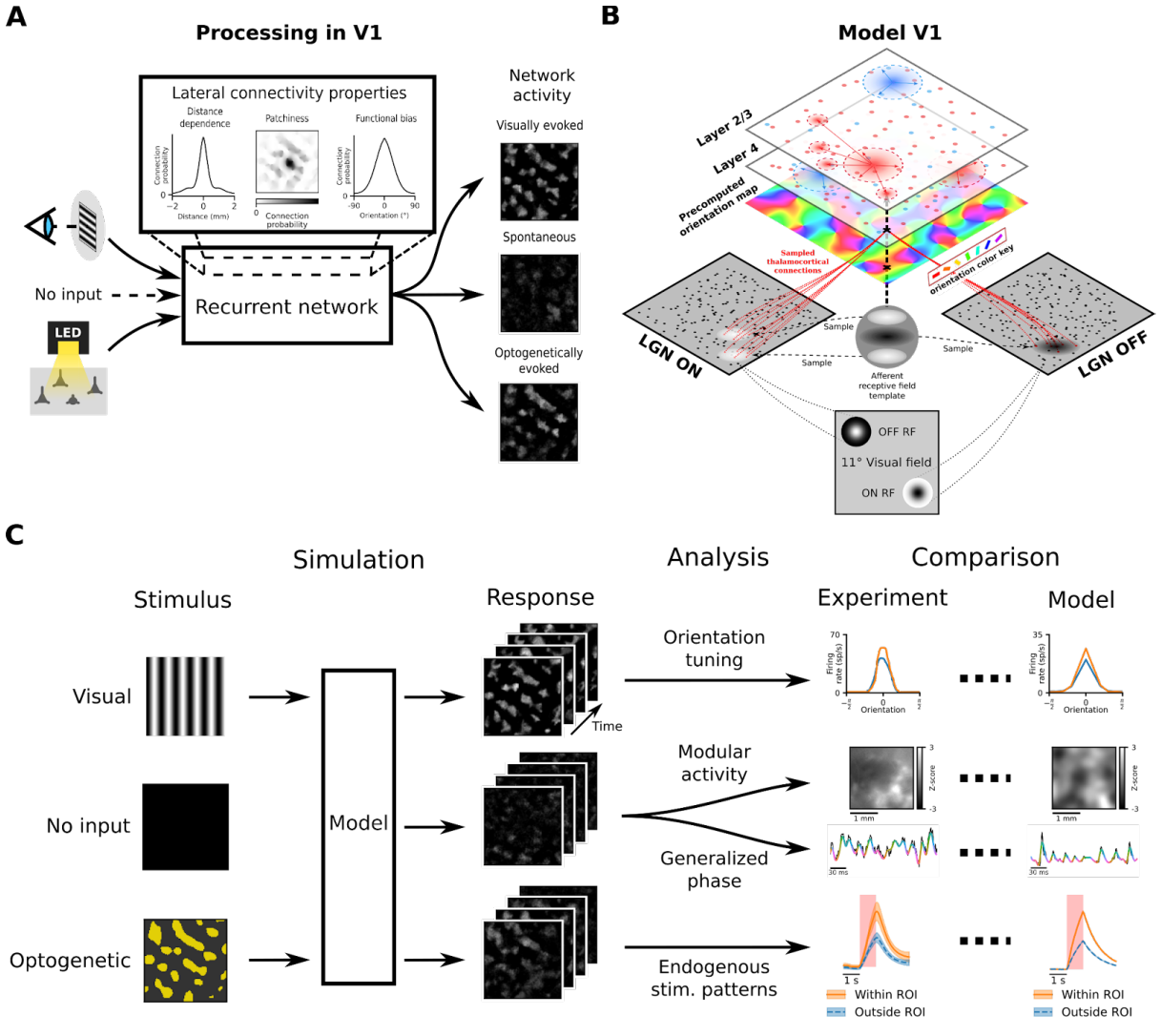

Figure 1: Common neural substrate underlies a range of visually evoked, optogenetically evoked, and spontaneous phenomena (A) Hypothesis: the interaction of distance dependent, patchy, orientation-biassed horizontal connectivity in Layer 2/3 with recurrent cortical connectivity underpins spontaneous, and visually and optogenetically evoked cortical responses. **(B)** Schematic of the V1 model: thalamocortical connections to cortical Layer 4 from ON and OFF LGN cells are sampled based on a precomputed orientation preference map. All cortical neurons make local connections, while only Layer 2/3 neurons make long-range intra-layer horizontal connections (see Methods). See Methods for the functionally specific rules of connectivity. **(C)** Computational approach: the simulated responses of neurons of a single parameterisation of the V1 model under multiple stimulation paradigms (no stimulus, visual or optogenetic) are recorded and analysed according to a range of experimentally measured criteria and compared to experimental results (illustrative experimental data scraped from (*12*, *25*) or adapted from (*10*, *26*) with permissions obtained via Rightslink and under the GNU licence, respectively).

Spontaneous travelling waves exhibit iso-oriented bias of propagation that depends on functionally biassed connectivity in layer 2/3

Voltage-sensitive dye and local field potential (LFP) studies have shown that cortical activity can propagate as travelling waves on both macroscopic and mesoscopic scales under various conditions (*4–6*). To determine if the model's spontaneous activity exhibits wave-like patterns we generated a synthetic LFP signal from the neurons' input current (*27*), which we then convolved with a 2D Gaussian (SD=250 μm) to account for the spatial pooling of LFPs in electrode recordings (*28*) (see Methods). As shown in Figure 2A, the synthetic LFP signal propagates across the model cortical surface as a STW.

We next applied the Generalized Phase analysis (*7*, *18*) to compute the instantaneous phases of a wideband filtered signal (Figure 2B), yielding the distribution of wavelengths and propagation speeds of the synthetic LFP (see Methods). The peak of both the distribution of firing rates and coefficients of variation (CV) match well the experimental data (Figure 2CD). Prior to convolution, the wavelengths of our synthetic LFP signal are significantly higher than in the spatially shuffled signal, demonstrating that the signal is indeed spatially structured (Figure 2F). After applying the Gaussian convolution to account for spatial pooling, the distribution of the wavelengths in the signal closely matches experimental data at high and intermediate wavelengths. However, we observe a greater proportion of low wavelengths, likely due to the limited simulated cortical area and downsampling of neural density, which increase global network synchronisation. The distribution of propagation speeds also lies within the inter-subject variability identified by Davis *et al.* (*7*, *18*) (Figure 2G).

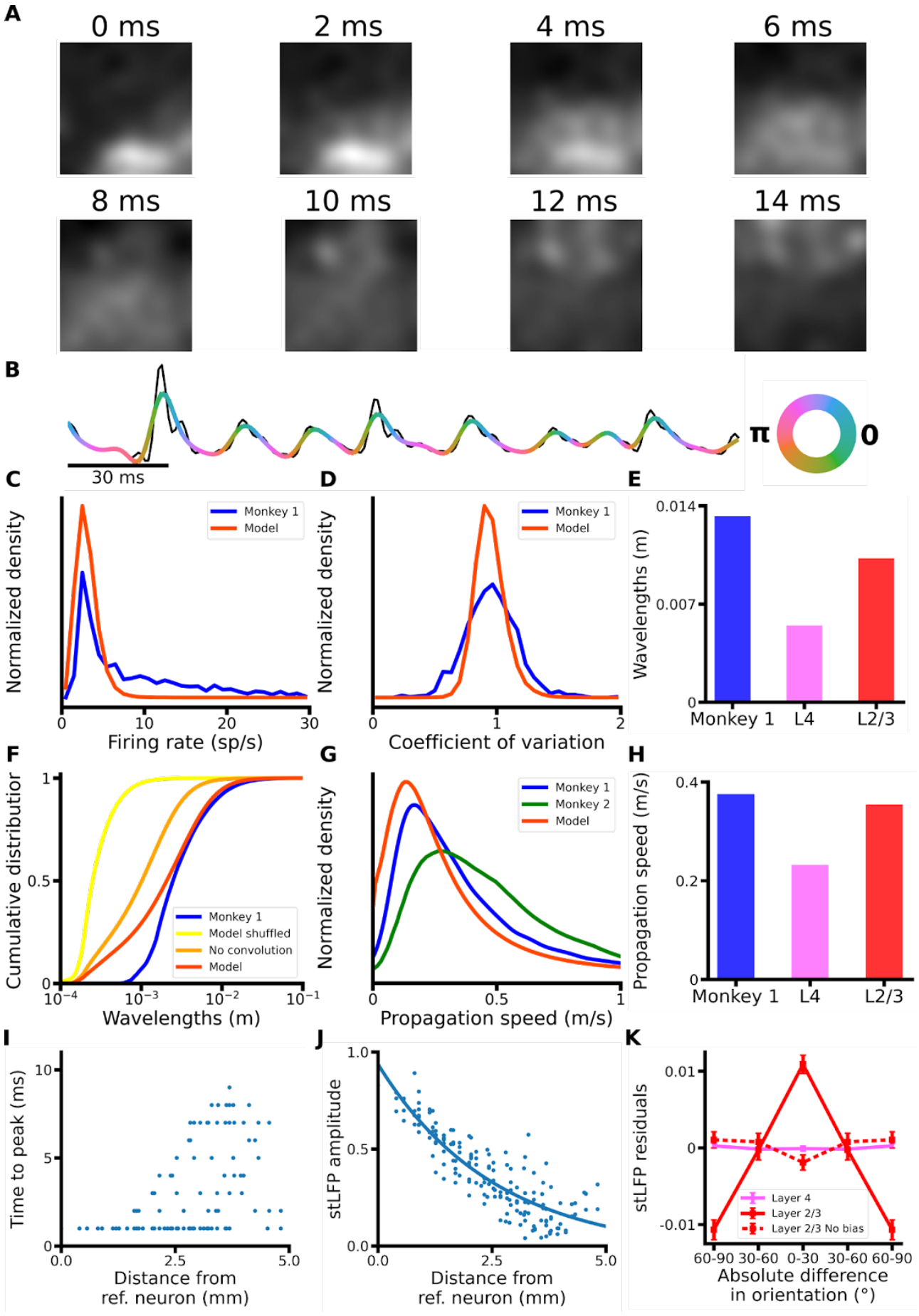

Figure 2: STW in the V1 model (A) Example frame sequence of the generated LFP signal of the model Layer 2/3 spontaneous activity showing propagation of a STW. **(B)**

Synthetic LFP signal (black) and corresponding generalised phase analysis, with the colour indicating the instantaneous phase. **(C)** Distribution of the firing rates of the neurons in Layer 2/3 of the V1 model (Red) and analogous experimental data in marmoset (Davis & al. 2021 (*18*); Blue). **(D)** Same as **(C)**, for the coefficient of variation of the inter-spike-interval. **(E)** The average wavelengths for the model layers 4 (pink) and 2/3 (red) and for the experimental data of Davis & al. 2021 (*18*) (blue). **(F)** Cumulative distributions of the wavelengths of the simulated LFP signal in the model Layer 2/3 before (orange) and after (red) its spatial convolution with a Gaussian. The cumulative distributions of the spatially shuffled signal is shown in yellow, and the cumulative distribution of the LFP signal recorded in the experimental data of Davis & al. is shown in blue (*18*). **(G)** Propagation speeds distribution of the LFP signal in the model (red) and in 2 marmosets (green: scraped from Extended Data 2d 'Monkey T' in Davis et al. 2020 (*7*); blue: data from Davis et al. 2021 (*18*)). **(H)** Same as **(E)**, for the average propagation speeds. **(I)** The peak times of the spike-triggered LFP for each spatial location plotted against their distance from one example reference neuron from layer 2/3. **(J)** The amplitudes of the spike-triggered LFP for each spatial location in relation to their distance from one example reference neuron from layer 2/3, and the corresponding exponential fit (solid blue line). **(K)** The average of the spike-triggered LFP residuals for layers 4 (pink) and 2/3 (red, solid: default configuration, dashed: configuration without functional bias in horizontal connections) across reference neurons and recording sites, binned according to their orientation preference differences. Error bars: 95% confidence interval.

Next we studied the relationship between spontaneous wave propagation and the intrinsic functional maps identified by Nauhaus *et al.* (*8*) in cats and macaques. They found that the delay of the peak of the spike-triggered LFP (stLFP) increased with distance from the reference electrode where spikes were recorded. Crucially, they also observed significantly higher amplitudes of stLFP residuals at recording sites with orientation preference congruent to the reference electrode, than for sites with orthogonal preference, indicating functionally specific wave propagation. We repeated their analysis using the spike trains of 269 model neurons as reference to compute the stLFPs (see Methods). We found that, for a given reference neuron, iso-oriented recording sites had significantly higher stLFP residuals than recording sites in orthogonal domains ($t(286) = 24.07$, $p < 0.001$; see Methods) (Figure 2K). Overall these findings indicate that cortical STW propagate preferentially towards iso-oriented domains in the model as observed by Nauhaus *et al.*, confirming that we successfully account for functionally specific spontaneous V1 dynamics. Furthermore, we performed the same analysis after removing the functional bias in the long-range excitatory connectivity in the model layer 2/3. After this manipulation, the stLFP is no longer higher for iso-oriented recording sites than for orthogonal recording sites (Figure 2K), demonstrating that functionally specific connectivity is critical for the iso-oriented bias of STW propagation.

Due to inaccessibility to imaging techniques, STW have not been yet analysed in layer 4 of V1. We hypothesised that due to the absence of functionally specific long-range lateral connectivity in layer 4 (*29*), the propagation of STWs in layer 4 would lack orientation bias. Indeed, we find that the stLFP residuals for recording sites of orientation preference

congruent to the reference neurons' were not significantly different to stLFP at orthogonally oriented sites ($t(290) = -1.60$, $p = 0.11$) (Figure 2K). Interestingly, we also find that propagation speeds and wavelengths in model layer 4 are lower than in layer 2/3 (Figure 2EH), which we attribute to shorter-range connectivity in layer 4 which requires activity to make multiple synaptic jumps to propagate to longer distances.

Functional specificity of cortical connections dictate correlation structure of spontaneous activity

Activity of both inhibitory and excitatory neurons is correlated over multiple millimetre distances, with excitatory activity resembling orientation preference maps in ferret V1 (*10*, *22*). To test the presence of this phenomenon in the model we have replicated the analysis of Smith et al. (*10*): first, we accounted for the spatiotemporal blurring of the underlying neural signal due to calcium imaging (Figure 3A; Methods; Figure S7) and subsequently calculated correlation maps (CMs) for each cortical position (Figure 3C), by correlating the activity time course at the given "seed" cortical position to the activity time courses of all other cortical positions.

We observe long-range correlations across the cortex, where excitatory CMs with seeds at iso-oriented positions in the orientation map were near-identical (Figure 3C), in line with ferret data (*10*). We also replicated the findings that excitatory CMs match inhibitory CMs (Figure 3D) and that excitatory CMs exhibit high similarity (see Methods) to the orientation preference maps and inhibitory CMs regardless of seed position (Figure 3E (left) and F) (*10*). Crucially, the orientation map similarity diminishes when we remove the orientation bias of Layer 2/3 long-range horizontal connections (Figure 3E (right), 4F), further underlining the importance of the functional biassed lateral connectivity in shaping spontaneous cortical dynamics.

Next, replicating the findings of Kenet et al. (*30*), we reconstructed the orientation preference map from excitatory spontaneous activity by fitting a circular Self-Organizing Map (SOM) to excitatory CMs (Figure 3G), demonstrating that the orientation preference encoding can be fully recovered from the correlations of spontaneous activity. Finally, the model accurately matches several key metrics of spontaneous ferret V1 activity (*10*, *22*) (Figure 3H): the degree of similarity of excitatory and inhibitory CMs; long-range correlations and correlation wavelength for both excitatory and inhibitory activity; and excitatory dimensionality and local correlation eccentricity.

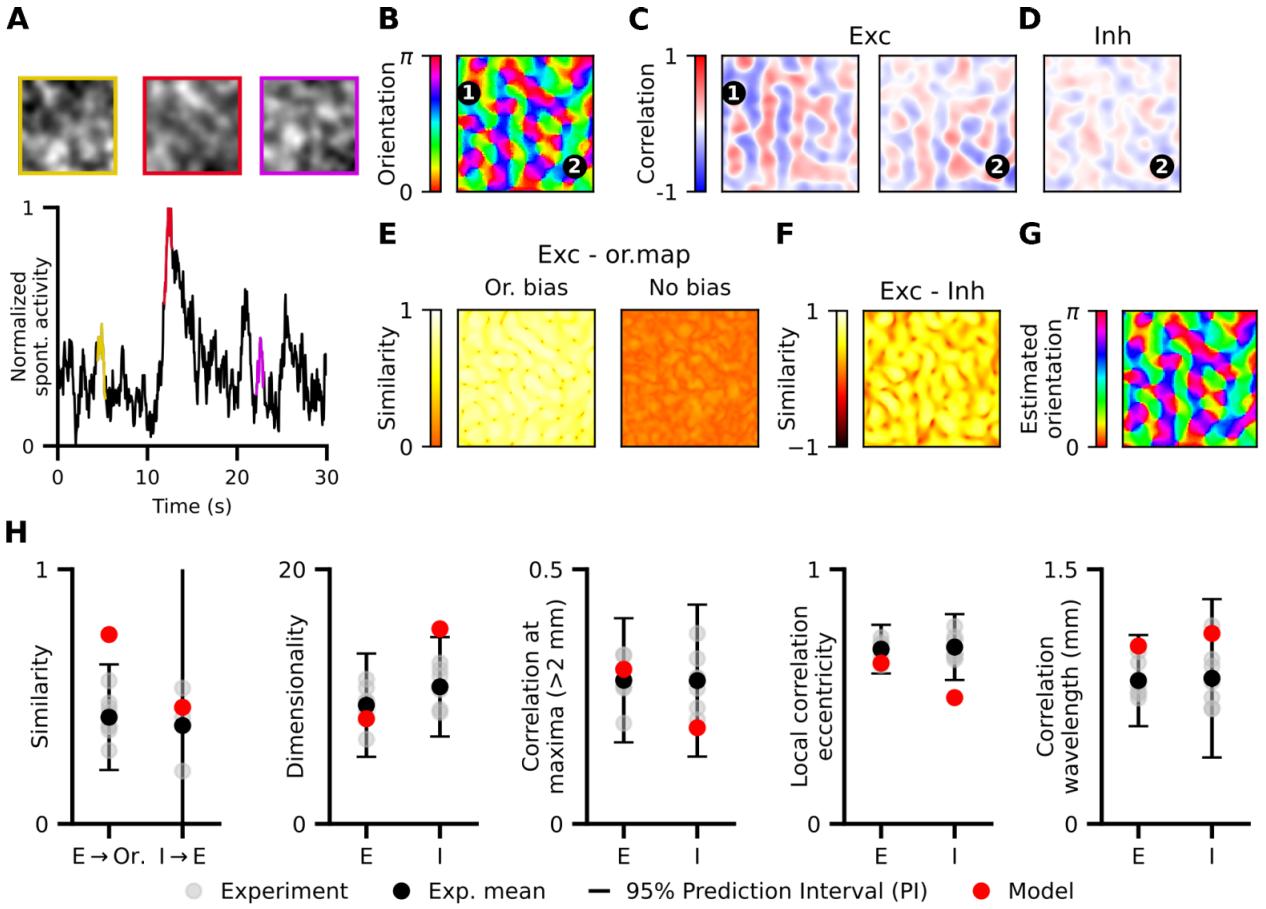

Figure 3: The structure of correlations in spontaneous activity is related to orientation maps (A) Example spontaneous activity events in the simulated visual cortex calcium imaging recordings. The colour border indicates the dominant orientation preference of activated neurons. **(B)** Orientation map with two iso-oriented points (1,2) and **(C)** correlation maps (CMs) of excitatory activity with seeds at those points. The CMs with iso-oriented seeds are similar. **(D)** CMs of inhibitory activity are similar to CMs from excitatory activity. **(E)** (left) Similarity between CMs at each seed point and the orientation map. Similarity is consistently high regardless of seed position. (right) Removing the orientation bias of lateral connections decreases similarity. **(F)** Similarity of excitatory and inhibitory CMs is also high, regardless of seed position. **(G)** A circular SOM fitted to spontaneous excitatory CMs predicts the structure of the orientation map. **(H)** For a wide range of metrics recorded in the ferret cortex (*10*, *22*), excitatory and inhibitory activity in the model lies within experimentally recorded values. Experimental data scraped from Smith et al. (*10*) Supplementary Figure 5g, Mulholland et al. (*22*) Figure 4c,e,g,j, 5f.

Iso-orientation biassed layer 2/3 connectivity boosts response to optogenetic stimulation congruent with orientation maps

We next investigated the V1 model's response to optogenetic stimulation, modelling stimulation from cortical surface in ferret V1 (Figure 4A). To do so, we used a brain-machine-interface (BMI) model we recently developed (*31*), that incorporates an LED array, light propagation through neural tissue, and channelrhodopsin dynamics (see Methods; Figure S6). The BMI model determines the current injected into each V1 neuron

through the channelrhodopsin channels in response to arbitrary light stimulation patterns. Subsequently the network's response to the optogenetic input can be simulated.

First, we replicated findings from a study that utilised an analogous optogenetic stimulation setup to modulate ferret V1 with homogeneous full-field stimulation (*14*). We calibrated the intensity of optogenetic stimulation such that the time course of a synthetic analog of the calcium imaging signal derived from the model's activity (see Methods) aligned with its biological counterpart ((*14*); Figure 4B). Experimentally, CMs derived from responses to full-field optogenetic stimulation closely resemble those derived from spontaneous activity (*14*). Consistent with these results, in the model CMs from full-field optogenetic activation closely matched spontaneous CMs (Figure 4C), irrespective of seed position (Figure 4D). The mean similarity of spontaneous and opto-response correlation maps was within the range of experimentally measured values (Figure 4E). As with spontaneous activity, the full-field opto-response CMs showed high similarity to the orientation map, but removing the orientation bias of long-range connections from the model decreased the similarity to chance level, demonstrating that the functional biases in later-connectivity mediate the link between orientation maps and optogenetically evoked activity (Figure 4F; see Methods).

Next we replicated Mulholland et al.'s (*12*) experiments that used a thresholded CM seeded at an arbitrary position (endogenous stimulation pattern - see Methods) as optogenetic stimulation pattern (Figure 4G bottom left). Since CMs are highly correlated with the orientation map, they predominantly stimulate cortical positions within a narrow band of orientation preferences (Figure 4G, top left). Following Mulholland et al. (*12*), we also created surrogate stimulation patterns that match the spatial statistics of endogenous patterns, but are unaligned with the spontaneous CMs (see Methods) to serve as controls. Finally, we define the region-of-interest (ROI) for the given optogenetic stimulus as the area of cortex beneath the stimulation pattern (Figure 4G; Methods).

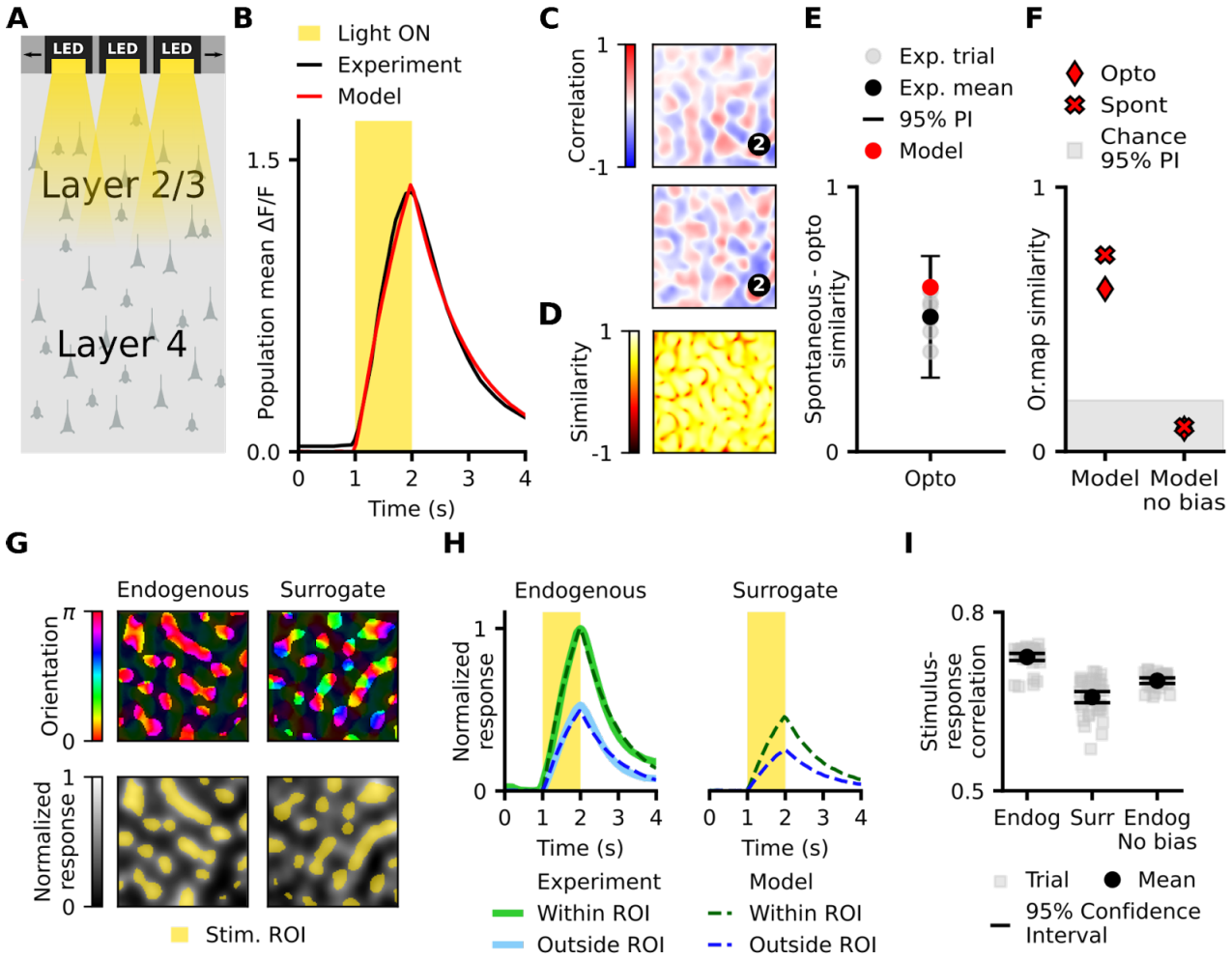

Figure 4: Full-field and patterned stimulation evokes structured model responses **(A)** Schematic of optogenetic stimulation of model layer 2/3 neurons using a 400x400 LED array (see Figure S6 for a detailed description). **(B)** Mean simulated population response to full-field optogenetic cortical stimulation matches experimental data (*14*). **(C)** CMs calculated from spontaneous activity (top) and response to optogenetic stimulation (bottom) at the same seed position are similar (similarity index = 0.64). **(D)** Spontaneous and optogenetic response CMs are highly correlated to each other, regardless of seed position. **(E)** The mean correlation between spontaneous activity and optogenetic responses matches experimental results. **(F)** The similarity of both spontaneous and optogenetic correlation maps to the orientation map decreases to chance level when we remove the orientation bias of long-range connections. **(G)** (left) Endogenous stimulation patterns based on CMs and (right) statistically matched surrogate patterns uncorrelated with CMs. **(H)** The model matches the experimentally measured (*12*) maximum-normalised mean population response to endogenous stimulation both within and outside the stimulation ROI (left). Stimulating with surrogate patterns evokes a weaker activation compared to the endogenous stimulation response (right). **(I)** Correlation between the stimulation pattern and evoked network activity pattern is higher for endogenous stimuli than for surrogate stimuli, in line with ferret experiments (14)**.** Removing the orientation bias from long-range connections decreases the endogenous stimulus-response correlation towards the level of surrogate stimulus responses.

Experimental data scraped from: Mulholland et al. (*14*) Figure 2c for (B), Supplementary Figure S10c for (E); Mulholland et al. (*12*) Figure 5k for (H).

Stimulating with endogenous patterns, the model matched the maximum-normalised time course of ferret V1 activation (*12*) both within and outside the stimulation ROIs (Figure 4H, left), confirming its ability to account for the spatio-temporal dynamics of V1 responses to patterned optogenetic stimulation. Consistent with the results of Mulholland et al. (14), we found that endogenous patterns evoked responses in the model that are stronger and more correlated to the stimulation patterns than those evoked by surrogate stimuli (Figure 4HI). We hypothesised that this is because aligned stimulation amplifies network responses via functionally specific recurrent connectivity, while unaligned stimulation fails to effectively engage this circuitry. Consequently, endogenous stimulation more strongly activates the winner-take-all mechanisms in layer 2/3, leading to stronger, more correlated responses. In support of our hypothesis, removing the orientation bias of layer 2/3 lateral connections reduced the stimulus-response correlation for endogenous stimuli to a level close to that evoked by surrogate stimuli (Figure 4I, endogenous no bias condition).

Orientation specific connectivity is necessary for sharpening of V1 response to optogenetic stimulation

Having access to responses of all neurons within the 5x5mm section of modelled cortex, we wished to gain deeper insight into how optogenetic stimulation engages the functionally specific cortical network. The spatiotemporal blurring effect of the calcium imaging readout underestimates the precision of neural responses in relation to stimulation, both spatially and temporally (Figure 5A,B). Therefore, we opted to perform all subsequent analyses directly on model spike responses.

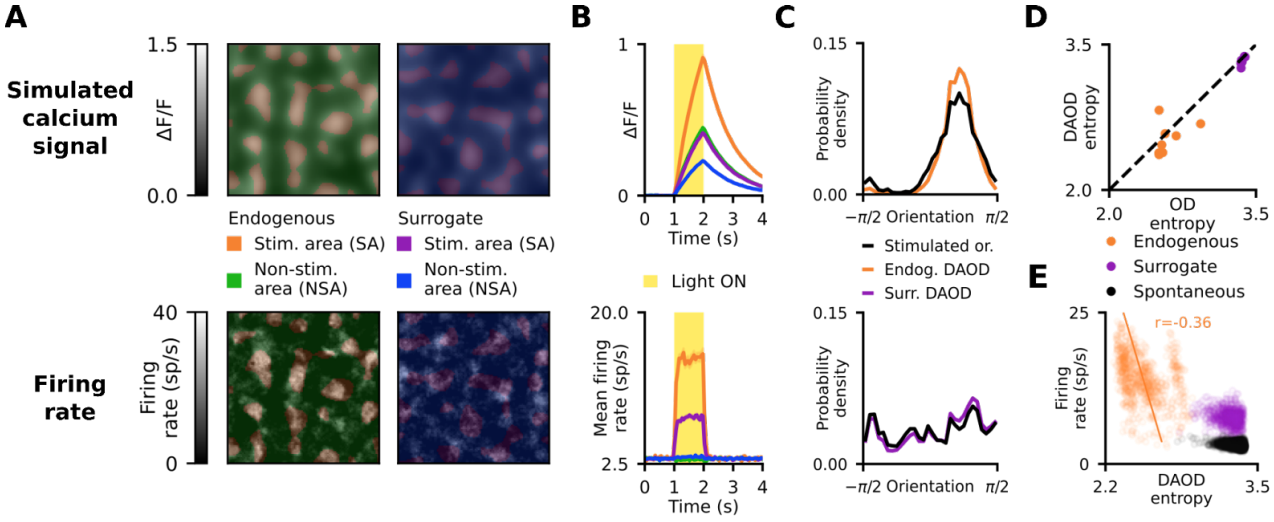

Figure 5: Sharper orientation tuning of optogenetic stimulation responses compared to stimulation patterns (A) Example stimulation patterns (endogenous and surrogate) and corresponding responses at the end of the 1s stimulation period shown for raw spiking data (bottom) and simulated calcium imaging signal (top). **(B)** Trial mean of stimulation responses within and outside the stimulated areas, showing the spatiotemporal smoothing effect of the calcium imaging readout. **(C)** The mean Distribution of Activity

across the Orientation Domain (DAOD) (see Methods) over the stimulation period and trials is more sharply oriented for both endogenous (orange) and surrogate (purple) stimuli, than the distribution of orientation preferences (OD) in the stimulated area. The plot shows the DAOD for a single endogenous/surrogate pattern. **(D)** Entropy of mean DAOD is consistently lower than the OD entropy across 14/16 stimulation patterns, showing that the activity due to stimulation is more sharply oriented than the stimulated area itself. **(E)** Entropy of DAOD is closely linked with firing rate - activity snapshots with higher activity exhibit sharper activations for both endogenous/surrogate stimulus responses and spontaneous activity (Pearson correlation $r_{endogenous}$=-0.36, $r_{surrogate}$=-0.20, $r_{spontaneous}$=-0.27). The points represent DAOD histograms pooled across all stimuli, trials and stimulation time points.

In light of our previous findings, we hypothesised that orientation-biassed cortical circuitry sharpens the orientation tuning of evoked activity relative to the functional bias of the optogenetically stimulated area. To test this, we stimulated the model cortex with 8 endogenous and 8 surrogate patterns (5 trials). We then calculated the Distribution of Activity across the Orientation Domain (DAOD) at each activity time point during stimulation: we binned the orientation domain, summed the activities of all cortical sites belonging to each bin, and normalised the resulting vector by dividing it by its sum (see Methods). We then compared the mean DAOD calculated across optogenetic stimulation response time points and trials to the distribution of orientation preferences within the stimulated ROIs (Figure 5C).

To test the existence of orientation tuning sharpening, we compared the entropies of the distribution of orientations under the stimulated regions and DAODs (Figure 5D), with lower entropies indicating broader tuning in the orientation domain. For most of the 16 tested stimulation patterns (8 endogenous, 8 surrogate), the entropy of DAOD distributions was lower than the entropy of the distribution of stimulated orientations, with the entropy difference between the DAOD and stimulated orientation distribution being significant compared to spatially shuffled controls ($p<10^{-17}$ for 14/16 stimulation patterns, see Methods). This result confirms our hypothesis that the network sharpens the response to optogenetic stimulation relative to the distribution of orientation directly stimulated, biassing its response towards the dominantly stimulated orientations, suggesting soft-winner-takes-all dynamics often hypothesised in cortical networks (*32*) .

Finally, we found an inverse relationship between DAOD entropy and firing rate across both spontaneous activity and responses to endogenous/surrogate stimulation - the higher the firing rate, the lower the DAOD entropy (Figure 5E). This effect was strongest for endogenous stimulation (Pearson correlation r=-0.49), but still present with surrogate stimulation (r=-0.28) and spontaneous activity (r=-0.27). This relationship is also consistent with soft-winner-takes-all dynamics, which would predict recurrent boosting of any spontaneous or externally induced patterns of activity aligned with the network's functional organisation due to the iso-orientation biassed connectivity.

Complex nonlinear interactions across the cortical space underlie population responses to optogenetic stimulation in V1

Experimental and modelling results discussed in the previous section suggest that stimulation patterns aligned with V1 functional organisation are more effective at driving cortical activity than equivalent unaligned patterns, which we hypothesise is underpinned by the functionally specific connectivity in layer 2/3. To understand these network phenomena more mechanistically, we performed simulations focusing on how lateral centre-surround interactions emanating from a single column shape the response to optogenetic stimulation. We stimulated the model in a circular area of variable diameter centred on a central orientation domain (Figure 6A), and analysed the resulting activations in the surrounding cortical region. We defined the not-directly-stimulated surround as the cortex beyond the largest tested circular stimulation area (300μm) plus an extra 100μm margin to exclude neurons potentially directly activated by scattered light (Figure 6B, left). We kept the total luminance input to the cortex constant by rescaling the stimulation intensity for each radius accordingly.

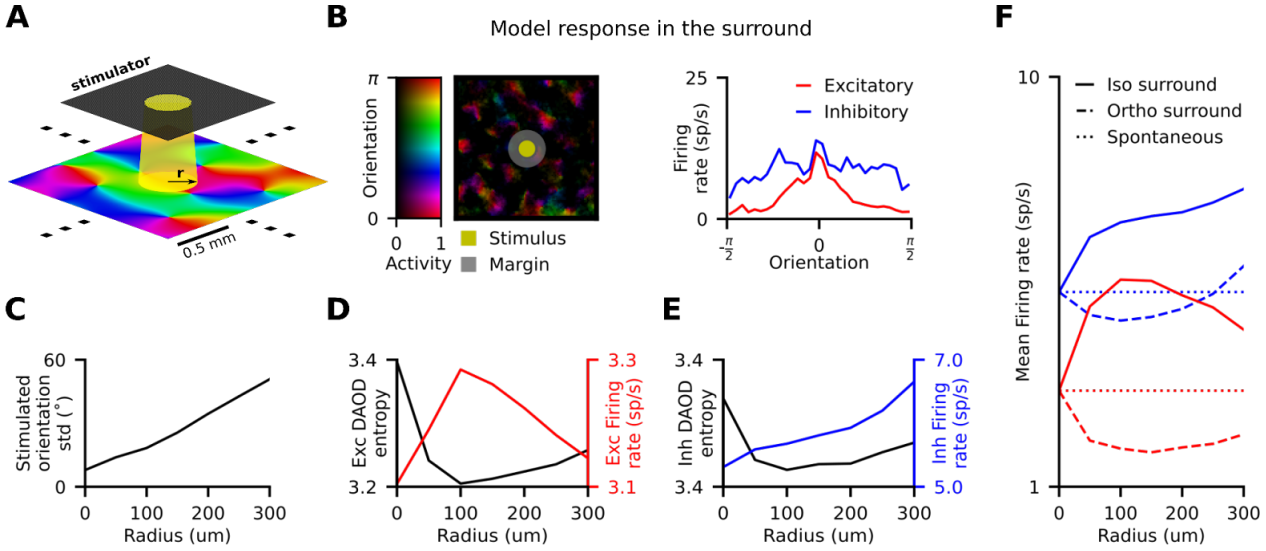

Figure 6: Central stimulation produces functionally specific nonlinear effects in the cortical surround (A) Localised optogenetic stimulation - we stimulate in a small circle with radii increasing from 50μm to 300μm in the middle of the simulated cortical region, targeting a cortical orientation column. **(B)** (left) Stimulation responses beyond the stimulated area. The central stimulated orientation column has horizontal orientation preference (red colour code). The activity in the surrounding cortex is biassed towards iso-oriented areas (red). (right) DAOD histograms for excitatory and inhibitory neurons in the non-stimulated cortex for the depicted frame (with entropies 2.9, 3.3). Activity of the excitatory population is much more sharply tuned than that of the inhibitory population. **(C)** The range of orientation preferences under stimulation ROIs increases with the increasing stimulation radius. **(D)** Excitatory firing rate rises to a maximum and subsequently begins falling, while **(E)** inhibitory firing rate in the surround scales monotonically with increasing radius. Both excitatory and inhibitory DAOD entropy inversely follows excitatory activation. **(F)** At the stimulation radius maximally exciting the surround, in iso-oriented regions both excitatory and inhibitory neurons show increased firing rate compared to spontaneous,

while in ortho-oriented regions both excitatory and inhibitory neurons exhibit decreased firing rates.

In line with iso-orientation biassed long-range lateral connectivity, we found that neurons in the surround of directly simulated cortex are biassed towards similar orientations as that of the stimulated column (Figure 6B, left). As we increase the radius of illumination, neurons from an increasingly broader range of orientations are directly stimulated (Figure 6C). Yet, the activity and the overall orientation selectivity of the excitatory response in the surround is non-monotonic (Figure 6D). Initially, increasing stimulation radius raises the mean activation of neurons in the surround (Figure 6D, red line), while decreasing their DAOD entropy (Figure 6D, black line). This mirrors the relationship between firing rates and selectivity observed in patterned stimulation (Figure 5E). This initial rise in selectivity is driven by the recurrent boosting of the dominantly stimulated orientation mediated by the iso-oriented long-range connectivity, and consequent inhibition of the non-dominant orientation domains, in analogous manner to the previous results on patterned optogenetic stimulation (Figure 4I). Crucially, as the stimulation radius, and hence the range of stimulated orientations increases, both the mean activity level and DAOD in the surround concomitantly flip their trends. This flip cannot be explained by the total input coming from the directly stimulated central area, where the total spiking output of excitatory cells increases monotonically (Figure S8DE). Instead, this non-monotonic effect is due to the expanding range of directly stimulated orientations, which gradually diminishes the aforementioned recurrent iso-orientation boosting, leading to reduced activity and less sharp orientation tuning in the surround (Figure 6D). The precise location of this inflection point is the result of a complex interplay between the spatial scale of the orientation map, the spatial extents of long-range excitatory and short-range inhibitory connections, and balance of excitation and inhibition in the network. Nevertheless, the existence of the inflection point at around 100μm radius is an important prediction of the model.

We next wished to understand the difference between how the stimulated centre engages populations of iso-oriented vs. ortho-oriented neurons in the surround, which receive substantially different input from the centre. We found that in the iso-oriented regions, inhibitory activity rose continuously, while mean excitatory activity mirrored the non-monotonic profile profile of the pooled analysis (Figure 6F, full lines). In contrast, in the ortho-oriented subpopulations, where the responses of both excitatory and inhibitory responses followed the non-monotonic U-shaped curve (Figure 6F, interrupted lines).

Afferent vs. lateral interactions ratio, conduction delays, and functional connectivity bias impact cortical waves and modular spontaneous activity

To gain understanding on how key aspects of the model impact the expression of investigated model phenomena we systematically manipulated several key model parameters (see Methods), while monitoring the various measures introduced earlier. The exhaustive results of this parameter search can be found in (Figures S10 and S11). Here we pinpoint the most interesting findings. Increasing the strength of the afferent

thalamo-cortical connections (TC strength) increases the spontaneous activity of the network (Figure S10A) and the mean propagation speeds of spontaneous waves (Figure 7A). We hypothesise this is due to the increase of the resting voltage level, which raises the likelihood of fast monosynaptic propagation of the signals over long distances. Because we found that the overall model activity has a strong impact on its dynamics (Figures 5, S10AEIM), in the following, we dissociate the impact of activity level from the impact of the remaining parameters. We do so by adjusting TC strength for each investigated parameter value combination to match the overall activity level of the base model (see Methods) (Figure S10B-D).

As expected, the propagation speed of the cortical activity decreases with increasing intra-laminar conduction delays, highlighting its association with horizontal connections (Figure 7B). Next, in Figure 7C-F we show that the orientation bias of travelling waves concomitantly changes with both the spontaneous and opto-evoked CMs similarity to the orientation map as we change model parameters, indicating a close association between these phenomena and the lateral connectivity substrate. Specifically, we find that decreasing the relative impact of the lateral vs. feed-forward connectivity (through increasing TC strength) is negatively associated with these three metrics (Figure 7C). They are also dependent on the E:I balance as increasing the strength of the layer 2/3 excitatory-to-inhibitory connections (L2/3 E→I strength) also induces a decrease in propagation bias and both similarities (Figure 7E). Finally, all three measures sharply increase as the orientation bias of long-range horizontal connections increases (L2/3 E→E bias, Figure 7F), underlining the importance of the functional selectivity of the long-range connections for the coexistence of STWs, modular spontaneous activity and optogenetically evoked responses.

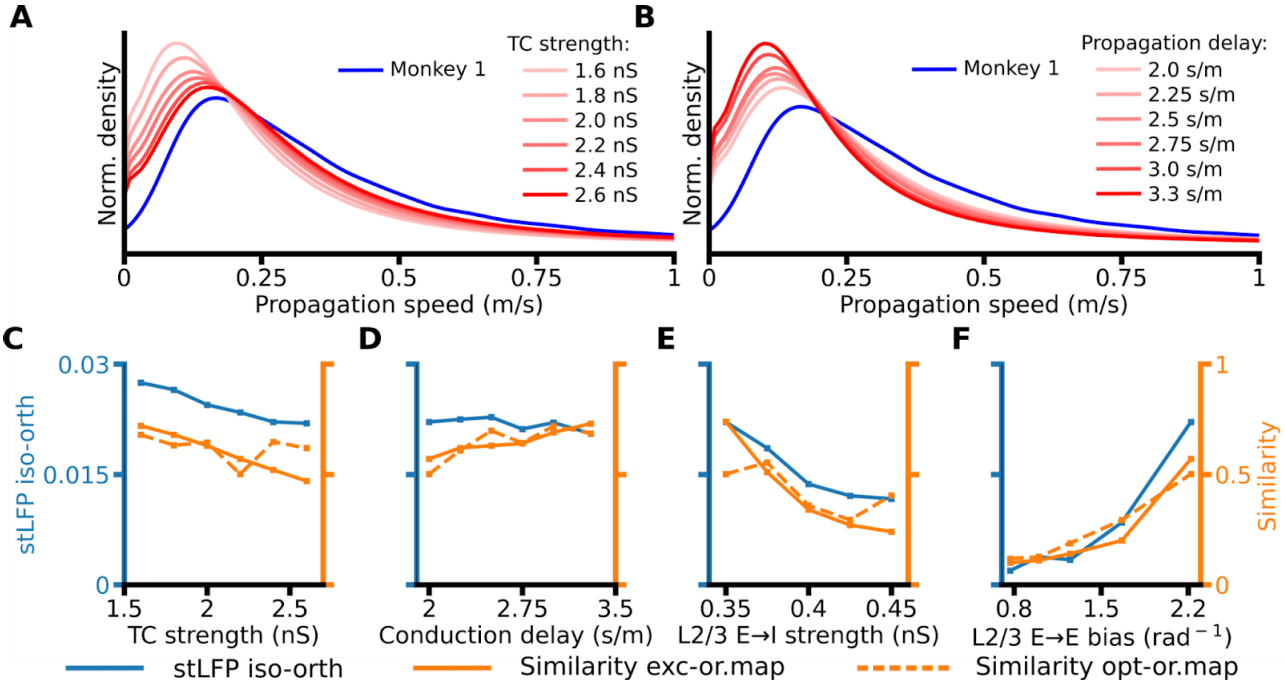

Figure 7: Impact of the parameters on model properties. (A) The distribution of propagation speeds for six parametrizations varying in TC strength. **(B)** Same, for six parametrizations varying in intra-laminar propagation delays. **(C)** For six parametrizations

varying in TC strength: (blue) stLFP residuals difference between recording sites with orientation preference congruent to the reference electrode and sites with orthogonal preference; (orange) similarity between the excitatory CMs and the orientation map (solid), and between the uniform full-field optogenetically evoked CMs and the orientation map (dashed). **(D)** Same, for six parametrizations varying in intra-laminar propagation delays. **(E)** Same, for five parametrizations varying in L2/3 E→I strength. **(F)** Same, for five parametrizations varying in L2/3 E→E bias.

Discussion

In this study we presented a unified computational model of V1 grounded in biologically established mechanisms and anatomical data, that explains an unprecedented range of phenomena across multiple dynamical regimes including visually driven processing, external optogenetic stimulation and spontaneous emerging activity patterns. The model for the first time reproduces: (i) iso-orientation biassed propagation of spontaneous waves, (ii) correlation of modular spontaneous activity to orientation preference maps, (iii) modular activity response to uniform full-field optogenetic stimulation that is correlated with modular spontaneous activity, and (iv) stronger responses to endogenous versus surrogate optogenetic stimulation patterns.

Our findings further the hypothesis that functionally specific lateral interactions in cortical layer 2/3 are key to the emergence of modular spontaneous activity, functionally specific propagation of spontaneous cortical waves and functionally specific responses to patterned optogenetic stimulation, bridging previously fragmented experimental observations into a coherent understanding of V1 dynamics.

This hypothesis is first corroborated by the finding that preferential propagation of STW into iso-oriented regions is abolished by removing the orientation bias of the long-range lateral connections in the model layer 2/3 (Figure 2K). Next, spontaneous activity in V1 (*10*) and other cortical areas (*33*) reflects the underlying functional organisation of the cortical circuitry. This manifests in modular events of higher activity which are correlated with the feature maps encoded across the cortical surface, such as orientation preference or ocular dominance maps in V1 (*34*). In the macaque, these events are more frequently aligned with ocular dominance maps (*34*), while in the ferret spontaneous activity events aligned with orientation preference are more frequent (*10*). In our model, lacking binocular processing, we demonstrate the encoding of orientation maps in spontaneous activity, and show that the long-range iso-orientation biassed lateral connectivity in layer 2/3 is necessary for the emergence of this phenomenon (Figure 3F). Finally, the similarity of the orientation map to both correlation maps derived from spontaneous activity and from activity evoked by full-field optogenetic stimulation in ferrets (*14*) suggests that spontaneous and optogenetically evoked activities are governed by the same underlying substrate. Indeed, we find that the iso-orientation bias of the layer 2/3 long-range connections is necessary for the emergence of modular activity in both stimulation conditions (Figure 4F).

Diving deeper into mechanisms of cortical dynamics, our analysis of the spatial scale of optogenetic stimulation revealed a non-linear relationship between the radius of optogenetic stimulation and cortical response (Figure 6DEF). We propose that this non-linear relationship is a consequence of the network operating within an inhibitory stabilised regime (*35*, *36*). We have shown that our model operates in this regime under both visual (10) and optogenetic stimulation (Figure S9), where increased input can paradoxically reduce the activity of both excitatory and inhibitory populations (*35*, *36*). Note that excitatory neurons in regions iso-oriented with the column at the centre of the opto-stimulated area receive stronger long-range input from this column due to the iso-orientation bias of the long-range E-to-E connectivity. In contrast, in ortho-oriented regions it is the inhibitory neurons that receive relatively stronger input, explaining the simultaneous reduction in the activity of both excitatory and inhibitory neurons in the ortho-oriented populations at the smaller stimulation radii which effectively drive a narrow range of orientations in the centre. These findings demonstrate that in cortical networks with heterogeneous, functionally specific connectivity, multiple functionally differentiated parts of the network can simultaneously operate in different regimes, leading to highly complex dynamical effects. This highlights the necessity to supplement simplified phenomenological models with simulations taking into account the full complexity of cortical interactions.

The critical assumption of this study is the existence of moderately iso-orientation biassed long-range connectivity in layer 2/3 of V1. The strongest evidence for functionally biassed intra-areal connectivity in V1 comes from mouse studies using a combination of optogenetics and patch-clamp recordings, which demonstrate a higher likelihood of connections between neurons with similar receptive fields (*37*, *38*). In mammals with columnar organisation of orientation preference, early studies combining intrinsic imaging and anatomical labelling provided evidence for long-range iso-orientation biassed connectivity in both cat (*15*, *16*) and tree-shrew (*39*). More recently, an optogenetics-based study confirmed these findings in ferrets, showing that the average orientation preference of synaptic inputs to layer 2/3 neurons aligns with their orientation preference (*17*). Moreover, while highlighting the heterogeneity of long-range connection targets, Martin et al. (*40*) show a clear bias toward synapses forming on iso-oriented targets in cat V1 neurons (see Figure 3, top-right histogram with SI peak above 0.5, indicating an iso-orientation bias). Overall, there is strong evidence across multiple species for a moderate iso-orientation bias in long-range layer 2/3 connectivity.

As with any model, we identify several key limitations that are primary candidates for future work. Due to the absence of feedback from higher visual areas, which has recently been shown to influence spontaneous activity (*41*), we cannot rule out that some of the studied phenomena could not be, at least partially, mediated by extra-areal interactions. Next, although the model also provides opportunity to study the interactions between spontaneous and visually evoked activity and their implications for perception (*7*, *9*, *23*), we have not explored these yet. Finally, the present model does not consider layer 5 and 6, which, with their extensive lateral arborisation, likely contribute to the spatial integration of information in V1.

Materials & Methods

1. V1 Model

The V1 model is a direct iteration of our previous modelling effort (*23*). It is composed of two layers corresponding to 5 x 5 mm patches of layers 4 and layers 2/3 of cat V1. The new model has higher density, with each layer containing 125 000 excitatory neurons and 31 250 inhibitory neurons. Layer 4 gets its input from a simplified model of LGN covering 6° × 6° of visual field and containing 14 400 neurons (see Methods: Retina & Lateral Geniculate Nucleus (LGN)). Layer 2/3 receives its feedforward input from Layer 4. In each layer, the number of connections is dominated by recurrent connections. The connections in Layer 4 are only local, while the excitatory connections in Layer 2/3 are both local and long-range. We offer detailed justification of modelling choices in our previous study (*23*). Here we will provide justification only for new or modified parameters (see Methods: Modifications from the previous model version:).

1.1 Neuron modelling

We simulate cortical neurons with adaptive exponential integrate-and-fire models (*42*):

$$\tau_{\mathrm{m}} \frac{\mathrm{d}V}{\mathrm{d}t} = -(V - E_{\mathrm{L}}) + \Delta_T \exp\left(\frac{V - V_T}{\Delta_T}\right) + R_{\mathrm{m}} g_{\mathrm{exc}}(E_{\mathrm{exc}} - V) + R_{\mathrm{m}} g_{\mathrm{inh}}(E_{\mathrm{inh}} - V) - w \quad (1)$$

Every time the membrane potential of a neuron crosses a threshold of -40 mV, a spike is generated and the membrane potential of the neuron is reset to a value V_r = -70 mV for a refractory period of 2 ms and 0.5 ms for excitatory and inhibitory neurons respectively. τ_m is the time constant of the membrane and is equal to 8ms for excitatory neurons and to 9 ms for inhibitory neurons. The leak potential E_L and the spike initiation threshold V_T are set respectively to -80 mV and -57 mV for excitatory neurons, and to -78 mV and -58 mV for inhibitory neurons.. The threshold slope factor ΔT of the exponential function is equal to 0.8 mV. The membrane resistance R_m is equal to 250 MΩ for excitatory neurons and to 300 MΩ for inhibitory neurons. The excitatory and inhibitory reversal potentials E_{exc} and E_{inh} are respectively set to 0 mV and -80 mV. The adaptation current w is further detailed in Table S2.

1.2 Retina & Lateral Geniculate Nucleus (LGN)

LGN neurons are modelled as leaky integrate-and-fire cells. They are driven by injected current computed by convolving stimuli in the model's visual field with a 3D spatiotemporal receptive field kernel based on LGN measurements by Cai et al. (*43*). This convolution is subsequently scaled by contrast and luminance gain to match experimental observations (*44*, *45*) of contrast and luminance saturation, as described by Antolik et al. (*23*). The baseline firing rate of LGN neurons is achieved by injecting Gaussian noise current into the neurons, such that the baseline firing rates of both ON and OFF LGN neurons match experimentally observed values (*45*).

1.3 Thalamo-cortical connections

Every neuron in Layer 4 receives an input from the LGN. The spatial pattern of the thalamo-cortical connectivity is modelled by the sum of a Gabor distribution and of a 2 dimensional Gaussian.

$$g(x, y, \lambda, \theta, \psi, \sigma, \gamma) = \exp\left(\frac{x'^2 + y'^2\gamma^2}{2\sigma^2}\right)(G + \cos(2\pi x'\lambda + \psi)) \tag{2}$$

$$x' = x\cos\theta + y\sin\theta$$
$$y' = -x\sin\theta + y\cos\theta$$

Where G represents the relative weight of the Gaussian, and is set at 0.085. The coordinates x and y of the positions of the neurons, as well as their phase preference ψ, are generated randomly. The orientation of the Gabor distribution θ is determined by the position of the neuron on a pre-computed orientation map. We set the aspect ratio γ of the Gabor distribution to 2.5, the spatial frequency λ to 0.8 cycles per degree, and the size σ to 0.17°.

Individual layer 4 excitatory and inhibitory cells receive connections from the LGN whose number is drawn from uniform distributions of respective boundaries of [90, 190] and [112, 168].

1.4 Cortico-cortical connectivity

Excitatory neurons in layer 4 receive 1000 synapses, whereas layer 2/3 neurons receive 2300 synapses. Inhibitory neurons receive 40% less connections than their excitatory counterparts. Cortical neurons receive excitatory and inhibitory connections following a ratio of 4:1. Layer 2/3 neurons receive 22% of their excitatory input through the feedforward connection originating in Layer 4. Furthermore, layer 4 neurons receive a direct feedback connection from Layer 2/3 corresponding to 20% of their total excitatory inputs, while the remaining excitatory synapses are formed by intra-laminar connections.

Recurrent connectivity in Layer 4, inhibitory connectivity in Layer 2/3, and excitatory feedforward connectivity from layer 4 to layer 2/3 are only local and distant-dependent. For each of these types of projections, the probability distribution of connections between pairs of neuron is given by the following equation:

$$pdf = p_{dist} + p_{func} \tag{3}$$

Where p_{func} and p_{dist} are respectively the functional and spatial components of the probability of connection. For these connections, p_{dist} follows a hyperbolic distribution:

$$p_{dist}(x) = \exp(-\alpha\sqrt{\theta^2 + x^2}) \tag{4}$$

with x the distance between the two neurons, and α and θ are the parameters shown in table 1 which were obtained by fitting connection probability data (see (*23*) for details) from Stepanyants et al. (*46*).

	α				θ			
	L4 Exc	L4 Inh	L23 Exc	L23 Inh	L4 Exc	L4 Inh	L23 Exc	L23 Inh
L4 Exc	0.0139	0.0148	0.0174	0.0197	207.7	191.8	154.4	131.5
L4 Inh	0.0126	0.0119			237.5	256.4		
L23 Inh			0.0149	0.0150			189.5	188.61

Table 1: Parameters of the hyperbolic distributions used to generate the local connectivity of the model. Rows refer to pre-synaptic populations, and columns to post-synaptic populations.

For recurrent connectivity in layer 4, the functionally specific component is modelled as a push-pull scheme, with excitatory connections being more likely to occur between neurons with correlated afferent receptive field templates (see Methods: Thalamo-cortical connections), and with inhibitory connections biassed towards neurons with anti-correlated receptive fields. A correlation c is computed between their receptive fields, here defined solely based on their afferent inputs from the LGN. This functional component is then the following:

$$p_{func_l4}(c) = \frac{1}{\sigma\sqrt{2\pi}} e^{\frac{-(c-\mu)^2}{2\sigma^2}} \tag{5}$$

With σ = 1.3, and μ = 1 or -1 respectively when the pre-synaptic neuron is excitatory or inhibitory.

For inhibitory connections in layer 2/3 there is no functional component and $p_{func_L23_inh}$ is therefore equal to 0 in equation (3). Feedforward projections from layer 4 to layer 2/3 are biassed for connecting neurons with similar orientation preferences. Their functional component is:

$$p_{func_l4\rightarrow l23}(\Delta o) = \frac{1}{\sigma\sqrt{2\pi}} e^{\frac{\Delta o^2}{2\sigma^2}} \tag{6}$$

Where Δo is the difference of orientation preference between the pre-synaptic and post-synaptic cells based on the pre-computed orientation map and with a standard deviation σ of 1.3 radians. The feedback connections from layer 2/3 to layer 4 are modelled in the same way as in equation (3). Their functional component has the same formula as equation (6) with σ is equal to 1.3 and 3 radians when targeting respectively excitatory and inhibitory neurons. Their spatial component is Gaussian:

$$p_{dist_l23\rightarrow l4}(x) = \exp(-\frac{x^2}{2\sigma^2}) \tag{7}$$

with σ = 100 μm. Finally, recurrent excitatory connections in Layer 2/3 consist of both local connections and long-range horizontal projection, the latter being orientation biassed. We model these connections with two spatial components as in Buzás et al. (*16*):

$$pdf_{l23} = p_{loc_l23} + \alpha p_{lr_l23} * p_{funct_l23} \quad (8)$$

where p_{loc_l23} and p_{lr_l23} represent the local and long-range spatial component, and follow the same formula as in equation (7) with σ respectively equal to 270 µm and 1000 µm. The functional factor p_{funct_l23} has the same formula as in equation (6) with σ equal to 0.45 and to 1.3 radians for connections targeting respectively excitatory and inhibitory cells. α defines the relative weight of the long range component and is equal to 4.

1.5 Synapses

All synapses of the model are modelled with an exponential decay according to the following formula:

$$g_{syn}(t) = \overline{g}_{syn} e^{\frac{-(t-t^*)}{\tau_{syn}}} \quad (9)$$

Where t* is the spike time and τ_{syn} is the time constant of the exponential decay and is equal to 1.5 ms for excitatory synapses and to 4.2 ms for inhibitory synapses. $\overline{g}_{syn}$ represents the weight of the synapses and differs according to the type of connection as shown in table S1C

Every synapse of the model also exhibits short-term plasticity through the Tsodyks-Markram model (*47*), with parameters shown in table S3. The delays of the intra-cortical connections of the model are implemented as the sum of two components, one constant and one distant-dependent. The propagation constant of the distant-dependent component is equal to 0.2 s/m for all intra-cortical connections. The constant delays are 1.4 ms and 0.5 ms for excitatory connections targeting respectively excitatory and inhibitory neurons, whereas inhibitory connections have constant delays equal to 1 ms. The delays of thalamo-cortical connections are drawn randomly from an interval of [1.4, 2.4] ms.

1.6 Modifications from the previous model version

The following changes from the previous model version (*23*) were made: The density was increased from 1500 neurons/mm^2 to 5000 neurons/mm^2 to reduce the downsampling of the number of neurons in the model relative to biological densities. It has been previously reported that a high enough density was required to accurately reproduce realistic STW in V1 (*18*), which we also empirically observed. To match the activity regime of the experimental data of Davis et al. (*18*) (see figure 2) and to compensate the reduction in spontaneous activity caused by the higher density, the strength of the thalamo-cortical connections was increased from 1.2 nS to 2.2 nS and the spike initiation threshold was decreased from -58 mV to -56 mV for inhibitory neurons. Furthermore, to compensate the excess of evoked activity that these changes created, we increased the strength of the inhibitory synapses from 1 nS to 2 nS as well as reduced their short-term plasticity recovery time constant in L4 from 70 ms to 30 ms, such that it now matches the other recurrent cortical connections, hence reducing the number of model parameters. Additionally, we have increased the strength of the recurrent and feedback excitatory-to-inhibitory connections targeting layer 4 from 0.22 nS to 0.35 nS so that it

matches the strengths of their equivalent in layer 2/3 further simplifying the model. Unfortunately, the effective synaptic strength has not been accurately determined experimentally at such a layer-to-layer and neuron type to neuron type level of granularity. We therefore tuned these parameters manually to achieve desired dynamical properties of the cortical network, but such that they remain within physiologically realistic ranges.

We have also decreased the standard deviation of the orientation bias of the layer 2/3 excitatory-to-excitatory connections long-range component from 1.3 radians to 0.45 radians, therefore making them more tuned to orientation in comparison to the previous model iteration. We found this increased bias was necessary to quantitatively accurately capture the functional propagation bias of STW and the alignment of the modular spontaneous activity on the network underlying functional organisation (see Figure 7F). Unfortunately, the exact strength of the orientation bias was never experimentally quantified due to the complexity of designing such experiments, but has been qualitatively demonstrated in several studies (*16*, *48*). We have also decreased the conduction delays from 3.3 s/m to 2 s/m, taking it closer to the mean value of 1.67 s/m but further away from the median value of 3.3 s/m observed in macaques that we used previously (*49*).

2. Data analysis

2.1 Coefficient of variation of the inter-spike-interval

For each neuron, we computed the coefficient of variation (CV) of its inter-spike-interval (ISI) as:

$$CV_{ISI}^2 = \frac{Var[ISI]}{\langle ISI \rangle^2}$$

2.2 LFP signal

To synthesise LFP signal from our point neuron population of L2/3 excitatory neurons we used the 'Reference Weighted Sum' proxy that has been developed for simulating the LFP signal of pyramidal neurons (*27*). This proxy uses a weighted sum of the inhibitory current and of the delayed excitatory current to estimate the participation of single neurons in the LFP signal of the population.

$$LFP = \sum_i^n I_{exc}^{(i)}(t - \tau_{exc}) - \alpha \sum_i^n I_{inh}^{(i)}(t - \tau_{inh})$$

With the delay of the excitatory current τ_{exc} equal to 6 ms, the delay of the inhibitory current τ_{inh} equal to 0 ms, and the coefficient α equal to 1.65. I_{exc} and I_{inh} represent respectively the input excitatory and inhibitory currents. We computed the LFP signal in a 100 x 100 grid representing the 5 mm x 5 mm area of the model, with each portion of the grid corresponding to the signal generated independently by a pool of n=12.5 neurons in average. We then normalised the LFP signal to transform it into a z-score. As experimental electrode recordings pool the LFP signal across several hundreds of micrometres (*28*), we convoluted our signal with a 2D Gaussian with a standard deviation of 5 units of the grid (corresponding to 250 μm).

2.3 Wave properties analysis

We applied the Generalised Phase (GP) analysis (*7*, *18*) on the computed three dimensional LFP signal of the 4mm x 4mm central portion of the model. We first applied a band-pass-band Butterworth filter (5-100 Hz, 4th order) on the computed LFP signal. We then computed the analytic signal after applying an Hilbert transform on the wideband filtered LFP signal. The instantaneous frequency of the signal was calculated as the time derivative of the phase ϕ of the analytical signal:

$$f_{inst} = \frac{\partial \phi}{\partial t}$$

As high frequencies in the signal induce sequences of n_t points with negative frequencies, we found these data points with negative instantaneous frequencies and performed a cubic interpolation along the temporal dimension on the phase of these n_t as well as on the phase of the next $2n_t$ time points.

The wavelengths of the signal were computed as the inverse of the magnitude of the spatial gradient of the phase of the signal at each time and space points:

$$wl = \frac{1}{|\nabla_{x,y}\phi|}$$

We then computed the propagation speed of the signal as the product of the wavelengths and of the instantaneous frequency of the signal:

$$v_{prop} = wl * f_{inst}$$

2.4 Spike-triggered LFP

We computed the Spike-triggered LFP (stLFP) from 316 reference excitatory neurons in the Layer 2/3 of the model following the procedure of Nauhaus et al. (*8*). Every reference neuron was located in the central 4 mm x 4 mm portion of the model. For each reference neuron, we then computed the stLFP as the average of the LFP signal over a 13 x 13 sub-grid of the original LFP grid, with 400µm of spacing. We then fitted the relationship between stLFP peak amplitude, and the distance between the neuron and the corresponding electrode with an exponential (see Figure 2E). We discarded from further analysis 27 neurons for which the explained variance of the fitting was lower than 0.5. We then computed the stLFP residuals by subtracting the expected stLFP amplitude (determined by the exponential fit) at each electrode from the actually measured amplitude. We assigned an orientation preference to each recording site based on the pre-computed orientation map of the model. Next, for each reference neuron, we binned the residual stLFP of the recording site based on the difference between their assigned orientation preference and the orientation preference of the neuron. We then averaged the stLFP residuals in each bin across recording sites and seed neurons to compute the orientation bias of the stLFP residuals.

2.5 Simulated calcium imaging signal

To facilitate comparisons with calcium imaging experimental data, we constructed a synthetic calcium imaging signal from our model recordings (see Supplementary Figure

S7). We recorded model spikes on a 4x4 mm grid with 40 μm spacing and binned them into 50 ms time bins, forming the basis of our neural signal. We next convolved the neural signal at each spatial position with a temporal kernel (*50*) that characterises the exponential decay of calcium fluorescence following spikes (τ=1s): $K = e^{-\frac{t}{\tau}}$

Next, to model light absorption and scattering of the fluorescence signals in the cortex, we convolved the signal with a spatial kernel generated using a beam-spread function model (*51*). Fluorescence was modelled as isotropic emission from a disk of 20μm diameter (representing the neuron) at a depth corresponding to the superficial region of cortical Layer 2/3 (150μm). Due to the lack of available scattering data for the ferret cortex, we based our coefficients on experimental measurements in mouse cortex (*51*). Finally, we applied a spatial Gaussian bandpass filter to our signal (σ_{low} = 26 μm, σ_{high} = 200 μm), to match the experimental calcium image processing pipeline of (*10*).

2.6 Correlation maps (CMs) and CM similarity

We constructed correlation maps (CMs) from the synthetic calcium imaging signal by calculating pairwise correlations across time between all pairs of spatial positions following Smith et al (*10*). This process resulted in a correlation map for each spatial position, effectively capturing the spatial organisation of spontaneous cortical activity.

Next, to quantify the similarity of each correlation map (CM) to the orientation map we computed the magnitude of the pairwise correlation coefficient between the CM and the real and imaginary components of the orientation map (Smith et al. (*10*)). Specifically, for a selected "seed" cortical position s, the similarity Sim(s) was calculated as follows:

$$Sim(s) = \sqrt{corr_x(\Re(O(x)), C(s,x))^2 + corr_x(\Im(O(x)), C(s,x))^2}$$

Here, Sim(s) represents the similarity at position s, C(s,x) is the correlation value at spatial position x of the CM with seed s, and O(x) is vector-summed orientation map at spatial position x.

We generated the chance level orientation map similarity distribution for our neural signal by calculating the synthetic calcium imaging signal for uniform random noise (with equivalent space and time dimensions as our spontaneous activity recording) and calculating the correlation map similarity for each spatial position in this recording.

Finally, we calculated the similarity between two distinct correlation maps (CMs) with the same seed position as the Pearson's correlation coefficient between the two maps. To prevent local correlations from inflating the similarity between the networks, we excluded all pixels within a radius of 400 μm around the seed position in both maps. We repeated this process for each seed position, replicating the analysis of Mulholland et al. (*22*).

2.9 Determining orientation preference with Self-Organizing Maps

To reconstruct the orientation preference map of the model cortex, we used a circular SOM with 40 nodes, analogously to Kenet et al. (*30*). We supplied the set of all correlation maps to the SOM as input features, and ran the algorithm for 1000 iterations using the publicly available pip *som-pbc* package. We subsequently assigned an orientation to each node in the SOM with a step of 4.5° (180° / 40), and estimated the orientation preference of each spatial position by standard vectorial summation.

Since this algorithm does not recover the absolute phase and direction of the assigned orientations relative to the orientation map, we evaluated the mean circular distance between the estimated orientations and the orientation map for both directions and 1,000 phase shifts from 0 to π. We subsequently selected the phase and direction with the smallest circular distance.

2.10 Prediction interval

To determine the range of values in Figure 3H into which new experimental observations would likely fall, we calculated the 95% prediction interval from the data of each metric. The prediction interval for data generated from a Gaussian distribution with unknown mean and variance is given as follows (*52*):

$$PI = \mu \pm T_a s_n \frac{\sqrt{n+1}}{\sqrt{n}}$$

where μ denotes sample mean, s_n sample variance, n the number of points, T_a the 100((1 − *p*)/2)th percentile of Student's t-distribution with $n-1$ degrees of freedom and $p = 0.95$ the confidence level.

2.11 Distribution of Activity across the Orientation Domain (DAOD)

To calculate Distribution of Activity across the Orientation Domain (DAOD) histograms for each frame of activity during the 1-second of simulated optogenetic stimulation we assumed orientation preference binned into 30 intervals (ranging from 0 to π). We added the activity at each cortical position into one of these bins based on the orientation preference at that cortical position, and normalised the binned activity to form a distribution of activities across the orientation domain. In some cases (Figure 5D-F), we only included in the analysis positions within a given stimulation pattern's ROI.

To determine if the entropy difference between the distribution of sampled orientations and the corresponding DAOD is statistically significant we tested the null hypothesis that the activations from which the DAOD is constructed do not depend on spatial position and thus orientation preference. To do so we created a population (n = 1000) of control DAOD distributions by spatially shuffling the activations from which the DAOD is calculated. Next we calculated the absolute difference between the entropy of each control DAOD and the

entropy of the distribution of sampled orientations, forming a control distribution. Finally we used a two-tailed Z-test to determine if the absolute entropy difference between the distribution of sampled orientations and the corresponding DAOD is significantly different from the control distribution.

2.12 Parameterizations used for studying the impact of model parameters

We modified the following four parameters of the model to explore how they influence the phenomena we investigate in this study: (i) the strength of the afferent thalamo-cortical connections (TC strength), (ii) the cortico-cortical connections conduction delays, (iii) the orientation bias of the layer 2/3 intra-laminar excitatory-to-excitatory connections (L2/3 E→E bias) computed as the inverse of the standard deviation used to derive the functional component in the layer 2/3 excitatory-to-inhibitory connectivity (see Methods: Cortico-cortical connectivity), and (iv) the strength of the layer 2/3 intra-laminar excitatory-to-inhibitory connections (L2/3 E→I strength). As parameters (ii-iv) impacted the overall activity of the model, we paired these modifications with a change in TC strength to match the mean activity in the model for each model parameterization:

Propagation delays		L2/3 E→E bias		L2/3 E→I strength	
Delay value (s/m)	TC Strength (nS)	Bias value (rad^{-1})	TC Strength (nS)	Strength value (nS)	TC Strength (nS)
0.2	2.2	0.77	2.2	0.35	2.2
0.225	2.1	1	2.3	0.375	2.5
0.25	2	1.25	2.36	0.4	2.7
0.275	1.9	1.67	2.38	0.425	2.9
0.3	1.75	2.22	2.4	0.45	3.05
0.333	1.6				

Table 2: Pairing of values of TC strength with other parameters modifications.

3. Optogenetic stimulation

To simulate the effects of optogenetic stimulation on the V1 model, we utilised a model of BMI setup we developed recently (*31*). Figure S6 summarises the five-tier structure of this optogenetic stimulator construct:

1. Stimulation patterns
2. 2D stimulator array of identical circular light sources at the cortical surface
3. Light propagation in the cortical tissue
4. Illumination-dependent ChrimsonR channelrhodopsin dynamics in transfected cells
5. Large-scale model of the primary visual cortex.

Since the model of the primary visual cortex is detailed in Methods V1 Model, we will only expand on steps 1-4 in this section.

3.1 Stimulation patterns

We define the region-of-interest (ROI) as the cortical area located beneath each stimulation pattern, with uniform stimulation intensity across active pixels in each pattern. We present 3 types of stimuli to the model cortex:

1. **Full-field stimulation** - ROI covers the entire array.
2. **Endogenous patterns** - ROI corresponds to regions in the correlation map (CM) surrounding its local maxima, resulting in orientation-specific stimulation (see Figure 4, pattern construction details below).
3. **Surrogate patterns** - equivalent stimulation patterns to endogenous patterns but uncorrelated with the orientation map.

With the goal of matching the stimulation protocols of Mulholland et al. (*12*, *13*) as closely as possible, we create the patterned stimuli as follows:

1. **CM selection:** We select CMs with seeds at positions with 8 equidistant orientation preferences (0, 22.5, 45, 67.5, 90, 112.5, 135, 157.5°) - this ensures a variety of different stimulation patterns all following intracortical structure.
2. **Endogenous ROIs**: We define the ROIs as the 25% highest correlation value pixels in each map. This is in line with the stimulation protocols of Mulholland et al. (*12*), who manually selected stimulation ROIs around CM maxima, resulting in approximately 25% of the cortical surface being stimulated (24.27% based on scraped data from Mulholland et al. (*12*) Figure 5i).
3. **Surrogate ROIs**: we rotate endogenous patterns by 90°, resulting in stimuli uncorrelated with the orientation map (mean orientation map similarity = 0.1 as opposed to 0.54 for endogenous stimuli).

To replicate the relative intensity difference used by Mulholland et al. (*12*, *13*) between full-field (10 mW) and patterned (7.6 mW) stimulation, we set the intensity of patterned stimulation to 76% of that used for full-field stimulation.

3.2 Stimulator array

We stimulate our in-silico cortical surface with a 4x4mm array of 10μm diameter circular light sources, centred on the cortex. We only stimulate layer 2/3 as the light intensity falloff from the surface is exponential, resulting in the amount of light reaching layer 4 to be negligible given the assumed illumination intensities. The light intensity at the cortical surface across the array is 3.0×10^{14} photons/s/cm^2.

3.3 Light propagation in cortical tissue

We simulate the propagation of light in the cortical tissue using the simulations of the 'Human Brain Grey Matter' model implemented in the LightTools software, assuming emitted light at 590 nm. The scattering and absorption properties of brain tissue are calculated using the Henyey-Greenstein model (*53*). Based on the work of Jacques et al. (*54*) we set the two key parameters of the model, *g* (anisotropy factor) and *MFP* (mean free path) to 0.87 and 0.07mm, respectively. The simulation results were tabulated into a 2D lookup table of light flux values at depth *d* and radial distance *r* relative to the centre of the light source to speed up simulations.

3.4 Channelrhodopsin model

To simulate the dynamics of the ChrimsonR channelrhodopsin in response to 590nm light stimulation, as used in the experiments of Mulholland et al. (*12–14*), we utilize the model of Sabatier et al. (*55*). The electro-chemical behaviour of the ChrimsonR protein is modelled using a 5-state Markov kinetic model (*56*), representing the conformations the protein can adopt. Transitions between these states, which the real system can chemically switch between, each have their own time constant and can be either thermally or photo-induced. Thermal transition time constants are fixed, while photo-transition time constants vary with light intensity. These transition time constants describe the linear differential equations governing the evolution of the proportion of channels in each state. The total conductance of all channels in a single neuron is then derived from the sum of conductances of open channels. We use model parameters fitted to 590 nm light stimulation experiments by Sabatier et al. (*55*) on ChrimsonR-expressing HEK293 cells.

Code Availability

The model, experiments and analyses were implemented through the Mozaik framework (*57*), freely accessible at https://github.com/CSNG-MFF/mozaik (version 0.4). To run the model one first needs to install Mozaik and its dependencies as indicated in the Mozaik Github repository, and then to download the implementation of model at https://github.com/CSNG-MFF/mozaik-models/tree/main/Rozsa_Cagnol2024 (version 1.0) and to follow the instructions to run the experiments presented in this study. We used NEST simulator (version 3.4) as the underlying simulation engine (*58*). We also made our model results and virtual experiment specifications available via a dedicated data store (http://v1model.arkheia.org) implemented in the Arkheia framework (*59*).

Bibliography:

1. J. R. Cavanaugh, W. Bair, J. A. Movshon, Nature and Interaction of Signals From the Receptive Field Center and Surround in Macaque V1 Neurons. *J. Neurophysiol.* **88**, 2530–2546 (2002).
2. C. D. Gilbert, A. Das, M. Ito, M. Kapadia, G. Westheimer, Spatial integration and cortical dynamics. *Proc. Natl. Acad. Sci.* **93**, 615–622 (1996).
3. F. Chavane, D. Sharon, D. Jancke, O. Marre, Y. Frégnac, A. Grinvald, Lateral spread of orientation selectivity in V1 is controlled by intracortical cooperativity. *Front. Syst. Neurosci.* **5** (2011).
4. L. Muller, F. Chavane, J. Reynolds, T. J. Sejnowski, Cortical travelling waves: mechanisms and computational principles. *Nat. Rev. Neurosci.* **19**, 255–268 (2018).
5. L. Muller, Propagating waves in thalamus, cortex and the thalamocortical system: Experiments and models. *J. Physiol.* (2012).
6. T. Sato, I. Nauhaus, M. Carandini, Traveling Waves in Visual Cortex.
7. Z. W. Davis, L. Muller, J. Martinez-Trujillo, T. Sejnowski, J. H. Reynolds, Spontaneous travelling cortical waves gate perception in behaving primates. *Nature* **587**, 432–436 (2020).
8. I. Nauhaus, L. Busse, M. Carandini, D. L. Ringach, Stimulus contrast modulates functional connectivity in visual cortex. *Nat. Neurosci.* **12**, 70–76 (2009).
9. Z. W. Davis, A. Busch, C. Steward, L. Muller, J. Reynolds, Horizontal cortical connections shape intrinsic traveling waves into feature-selective motifs that regulate perceptual sensitivity. *Cell Rep.* **43**, 114707 (2024).
10. G. B. Smith, B. Hein, D. E. Whitney, D. Fitzpatrick, M. Kaschube, Distributed network interactions and their emergence in developing neocortex. *Nat. Neurosci.* **21**, 1600–1608 (2018).
11. X. Huang, Y. M. Elyada, W. H. Bosking, T. Walker, D. Fitzpatrick, Optogenetic Assessment of Horizontal Interactions in Primary Visual Cortex. *J. Neurosci.* **34**, 4976–4990 (2014).
12. H. N. Mulholland, H. Jayakumar, D. M. Farinella, G. B. Smith, All-optical interrogation of millimeter-scale networks and application to developing ferret cortex. *J. Neurosci. Methods* **403**, 110051 (2024).
13. H. Mulholland, S. Tragenap, M. Kaschube, G. Smith, “Selective amplification of recurrent subnetworks in the developing visual cortex” (2024).
14. H. N. Mulholland, M. Kaschube, G. B. Smith, Self-organization of modular activity in immature cortical networks. *Nat. Commun.* **15**, 4145 (2024).
15. C. Gilbert, T. Wiesel, Columnar specificity of intrinsic horizontal and corticocortical connections in cat visual cortex. *J. Neurosci.* **9**, 2432–2442 (1989).
16. P. Buzás, K. Kovács, A. S. Ferecskó, J. M. L. Budd, U. T. Eysel, Z. F. Kisvárday, Model-based analysis of excitatory lateral connections in the visual cortex. *J. Comp. Neurol.* **499**, 861–881 (2006).
17. D. E. Wilson, D. E. Whitney, B. Scholl, D. Fitzpatrick, Orientation selectivity and the functional clustering of synaptic inputs in primary visual cortex. *Nat. Neurosci.* **19**, 1003–1009 (2016).
18. Z. W. Davis, G. B. Benigno, C. Fletterman, T. Desbordes, C. Steward, T. J. Sejnowski, J. H. Reynolds, L. Muller, Spontaneous traveling waves naturally emerge from horizontal fiber time delays and travel through locally asynchronous-irregular states. *Nat. Commun.* **12** (2021).
19. J. Luboeinski, T. Tchumatchenko, Nonlinear response characteristics of neural networks and single neurons undergoing optogenetic excitation. *Netw. Neurosci.* **4**, 852–870 (2020).
20. T. C. Potjans, M. Diesmann, The Cell-Type Specific Cortical Microcircuit: Relating Structure and Activity in a Full-Scale Spiking Network Model. *Cereb. Cortex* **24**, 785–806 (2014).
21. D. Cai, A. V. Rangan, D. W. McLaughlin, Architectural and synaptic mechanisms underlying coherent spontaneous activity in V1. *Proc. Natl. Acad. Sci. U. S. A.* **102**, 5868–5873 (2005).
22. H. N. Mulholland, B. Hein, M. Kaschube, G. B. Smith, Tightly coupled inhibitory and excitatory functional networks in the developing primary visual cortex. *eLife* **10**, e72456 (2021).
23. J. Antolík, R. Cagnol, T. Rózsa, C. Monier, Y. Frégnac, A. P. Davison, A comprehensive data-driven model of cat primary visual cortex. *PLOS Comput. Biol.* **20**, e1012342 (2024).
24. M. M. Taylor, D. Contreras, A. Destexhe, Y. Frégnac, J. Antolik, An Anatomically Constrained Model of V1 Simple Cells Predicts the Coexistence of Push–Pull and Broad Inhibition. *J.*

Neurosci. **41**, 7797–7812 (2021).
25. H. J. Alitto, W. M. Usrey, Influence of Contrast on Orientation and Temporal Frequency Tuning in Ferret Primary Visual Cortex. *J. Neurophysiol.* **91**, 2797–2808 (2004).
26. Z. W. D. Lyle Muller, Generalized Phase, *GitHub repository* (2020). https://github.com/mullerlab/generalized-phase.
27. A. Mazzoni, H. Lindén, H. Cuntz, A. Lansner, S. Panzeri, G. T. Einevoll, Computing the Local Field Potential (LFP) from Integrate-and-Fire Network Models. *PLOS Comput. Biol.* **11**, e1004584 (2015).
28. S. Katzner, I. Nauhaus, A. Benucci, V. Bonin, D. L. Ringach, M. Carandini, Local Origin of Field Potentials in Visual Cortex. *Neuron* **61**, 35–41 (2009).
29. K. S. Rockland, Anatomical organization of primary visual cortex (area 17) in the ferret. *J. Comp. Neurol.* **241**, 225–236 (1985).
30. T. Kenet, D. Bibitchkov, M. Tsodyks, A. Grinvald, A. Arieli, Spontaneously emerging cortical representations of visual attributes. *Nature* **425**, 954–6 (2003).
31. J. Antolik, Q. Sabatier, C. Galle, Y. Frégnac, R. Benosman, Assessment of optogenetically-driven strategies for prosthetic restoration of cortical vision in large-scale neural simulation of V1. *Sci. Rep.* **11**, 10783 (2021).
32. U. Rutishauser, J.-J. Slotine, R. J. Douglas, Competition through selective inhibitory synchrony. *Neural Comput.* **24**, 2033–52 (2012).
33. N. J. Powell, B. Hein, D. Kong, J. Elpelt, H. N. Mulholland, M. Kaschube, G. B. Smith, Common modular architecture across diverse cortical areas in early development. *Proc. Natl. Acad. Sci.* **121**, e2313743121 (2024).
34. D. B. Omer, T. Fekete, Y. Ulchin, R. Hildesheim, A. Grinvald, Dynamic Patterns of Spontaneous Ongoing Activity in the Visual Cortex of Anesthetized and Awake Monkeys are Different. *Cereb. Cortex N. Y. N 1991* **29**, 1291–1304 (2019).
35. M. V. Tsodyks, W. E. Skaggs, T. J. Sejnowski, B. L. McNaughton, Paradoxical Effects of External Modulation of Inhibitory Interneurons. *J. Neurosci.* **17**, 4382–4388 (1997).
36. H. Ozeki, I. M. Finn, E. S. Schaffer, K. D. Miller, D. Ferster, Inhibitory Stabilization of the Cortical Network Underlies Visual Surround Suppression. *Neuron* **62**, 578–592 (2009).
37. H. Ko, L. Cossell, C. Baragli, J. Antolik, C. Clopath, S. B. Hofer, T. D. Mrsic-Flogel, The emergence of functional microcircuits in visual cortex. *Nature* **496**, 96–100 (2013).
38. H. Ko, S. B. Hofer, B. Pichler, K. A. Buchanan, P. J. Sjöström, T. D. Mrsic-Flogel, Functional specificity of local synaptic connections in neocortical networks. *Nature* **473**, 87–91 (2011).
39. W. H. Bosking, Y. Zhang, B. Schofield, D. Fitzpatrick, Orientation selectivity and the arrangement of horizontal connections in tree shrew striate cortex. *J. Neurosci. Off. J. Soc. Neurosci.* **17**, 2112–27 (1997).
40. K. a C. Martin, S. Roth, E. S. Rusch, Superficial layer pyramidal cells communicate heterogeneously between multiple functional domains of cat primary visual cortex. *Nat. Commun.* **5**, 5252 (2014).
41. A. Morales-Gregorio, A. C. Kurth, J. Ito, A. Kleinjohann, F. V. Barthélemy, T. Brochier, S. Grün, S. J. Van Albada, Neural manifolds in V1 change with top-down signals from V4 targeting the foveal region. *Cell Rep.* **43**, 114371 (2024).
42. N. Fourcaud-Trocmé, D. Hansel, C. Van Vreeswijk, N. Brunel, How Spike Generation Mechanisms Determine the Neuronal Response to Fluctuating Inputs. *J. Neurosci.* **23**, 11628–11640 (2003).
43. D. Cai, G. C. DeAngelis, R. D. Freeman, Spatiotemporal receptive field organization in the lateral geniculate nucleus of cats and kittens. *J. Neurophysiol.* **78**, 1045–1061 (1997).
44. V. Bonin, The Suppressive Field of Neurons in Lateral Geniculate Nucleus. *J. Neurosci.* **25**, 10844–10856 (2005).
45. J. Papaioannou, A. White, Maintained activity of lateral geniculate nucleus neurons as a function of background luminance. *Exp. Neurol.* **34**, 558–566 (1972).
46. A. Stepanyants, J. A. Hirsch, L. M. Martinez, Z. F. Kisvárday, A. S. Ferecskó, D. B. Chklovskii, Local Potential Connectivity in Cat Primary Visual Cortex. *Cereb. Cortex* **18**, 13–28 (2008).
47. H. Markram, Y. Wang, M. Tsodyks, Differential signaling via the same axon of neocortical pyramidal neurons. *Proc. Natl. Acad. Sci.* **95**, 5323–5328 (1998).
48. Z. Kisvarday, Orientation-specific relationship between populations of excitatory and inhibitory lateral connections in the visual cortex of the cat. *Cereb. Cortex* **7**, 605–618 (1997).

49. P. Girard, J. M. Hupé, J. Bullier, Feedforward and Feedback Connections Between Areas V1 and V2 of the Monkey Have Similar Rapid Conduction Velocities. *J. Neurophysiol.* **85**, 1328–1331 (2001).
50. H. Lütcke, F. Gerhard, F. Zenke, W. Gerstner, F. Helmchen, Inference of neuronal network spike dynamics and topology from calcium imaging data. *Front. Neural Circuits* **7** (2013).
51. G. Yona, N. Meitav, I. Kahn, S. Shoham, Realistic Numerical and Analytical Modeling of Light Scattering in Brain Tissue for Optogenetic Applications. *eNeuro* **3** (2016).
52. *Predictive Inference* (Routledge, 2017; https://www.taylorfrancis.com/books/9780203742310).
53. L. C. Henyey, J. L. Greenstein, Diffuse radiation in the Galaxy. *Astrophys. J.* **93**, 70 (1941).
54. S. L. Jacques, Optical properties of biological tissues: a review. *Phys. Med. Biol.* **58**, R37-61 (2013).
55. Q. Sabatier, C. Joffrois, G. Gauvain, J. Chavas, D. Pruneau, S. Picaud, R. Benosman, “Modeling the Electro-chemical Properties of Microbial Opsin ChrimsonR for Application to Optogenetics-based Vision Restoration” (preprint, Neuroscience, 2018); https://doi.org/10.1101/417899.
56. A. Destexhe, Z. F. Mainen, T. J. Sejnowski, Synthesis of models for excitable membranes, synaptic transmission and neuromodulation using a common kinetic formalism. *J. Comput. Neurosci.* **1**, 195–230 (1994).
57. J. Antolík, A. P. Davison, Integrated workflows for spiking neuronal network simulations. *Front. Neuroinformatics* **7** (2013).
58. A. Sinha, R. de Schepper, J. Pronold, J. Mitchell, H. Mørk, P. Nagendra Babu, J. M. Eppler, M. Lober, C. Linssen, D. Terhorst, M. A. Benelhedi, A. Morrison, W. Wybo, G. Trensch, R. Deepu, N. Haug, A. Kurth, S. B. Vennemo, S. Graber, S. Spreizer, J. Gille, J. Vogelsang, M. Krüger, H. E. Plesser, NEST 3.4, version 3.4, Zenodo (2023).
59. J. Antolík, A. P. Davison, Arkheia: Data Management and Communication for Open Computational Neuroscience. *Front. Neuroinformatics* **12**, 6 (2018).